Flow Measurement and Instrumentation 66 (2019) 86–98

Contents lists available at ScienceDirect

Flow Measurement and Instrumentation

journal homepage: www.elsevier.com/locate/flowmeasinst

Water film thickness measurement system for oil-water pipe flow

A. Bonilla-Riaño[a,d,*], H.F. Velasco-Peña[b], A.C. Bannwart[a], H.-M. Prasser[c], O.M.H. Rodriguez[b]

[a] Department of Petroleum Engineering, University of Campinas, Campinas, SP, Brazil
[b] Industrial Multiphase Flow Laboratory (LEMI), Department of Mechanical Engineering, São Carlos School of Engineering, University of São Paulo (USP), São Carlos, SP, Brazil
[c] Institut für Energietechnik, ETHZ, Zürich, Switzerland
[d] Department of Research, Manuela Beltran University, Bogota, Colombia

A R T I C L E I N F O

Keywords:
Liquid-liquid flow
Film thickness measurement
Capacitive sensor
Planar sensor
Oil-water flow

A B S T R A C T

A new technique development for high spatial and temporal resolution film-thickness measurement in oil-water flow is presented in this work. A capacitance measurement system is proposed to measure thin water films or local water fractions near to the pipe wall. The measurement system is based in a planar sensor which is flexible and can be placed close to and following the curvature of the inner wall of the tube. Experimental results of the capacitive technique showed that the system is able to measure film thickness between 400 μm and 2200 μm. Dispersed and core-annular flows were studied in a vertical 12-m-height glass pipe with 50.8 mm of internal diameter, using mineral oil (860 kg/m3 of density and 220 mPa s of viscosity) and tap water. Local time-domain signals and axial and circumferential distributions of water film thickness near to the pipe wall and 3-D images of water film are presented. The measured film thickness, obtained by the proposed technique, was compared with that obtained through a camera-based imaging technique and the agreement was good, with a deviation less than 20%. The new technique allows the observation and characterization of average interfacial topologies in separated flows, and high frequency phenomena related to dispersed flows that occur in liquid-liquid flow near the pipe wall.

1. Introduction

Consumption of energy is expected to continue increasing in future years. In coming decades, fossil fuels will still be the primary source of energy, with 78% of total world energy consumption [1]. Some of these energy resources are harder to be extracted at the present than in the past [2]. The production challenges are related, in part, to oil reservoirs location, i.e., most of the new fields are offshore, at great depths under the sea and in some cases, to the high oil viscosity. The heavy-oil recovery matters are: the high flow resistance, the pressure drop, the need of heating and dilution during transport, lower market value and cost increase. This scenario has created an interesting research opportunity, aiming to develop new technologies improving the heavy oil recovery factor [3]. Several efforts had been done to explain the utility of reducing the friction in pipes. For example, Rodriguez et al. [4] increased the production rate in a full scale on-shore experiment using core-annular flow. Rodriguez et al. [5] studied the drag reduction phenomenon in dispersed flows and proposed a model to predict it.

There is growing attention on methods and technologies to improve the heavy oil transportation process [6]. Particularly, in methods focused on decreasing flow resistance to values low enough such that the pumping requirements and pipeline size reach viable values [7]. Lubricated transportation using core-annular flow and reverse emulsion (oil-in-water emulsion) have been recommended as techniques to reduce the pressure drop due to viscous effects [3,8]. Recently, reverse emulsion has been suggested as a promising solution to reduce the total pressure gradient and improve the gas-lift technique [9].

1.1. Core-annular flow

In core-annular flow, water flow is injected in the pipe in a way that an annular flow pattern is produced, with water near the wall surrounding an oil core. The water annulus keeps the oil from sticking to the pipe wall [3,10]. Therefore, the frictional pressure gradient is comparable to that observed in single-phase water flow, resulting in a significant decrease of pressure drop, but the more viscous the oil, the more intense the pressure-drop reduction [11]. According to experimental studies, for the core–annular flow pattern to occur the core phase should be much more viscous than the annulus phase and the in-situ volumetric fraction of the latter should be lower than 50%.

* Corresponding author. Department of Petroleum Engineering, University of Campinas, Campinas, SP, Brazil.
E-mail address: adriana.bonilla@gmail.com (A. Bonilla-Riaño).

https://doi.org/10.1016/j.flowmeasinst.2019.02.007
Received 4 July 2018; Received in revised form 23 November 2018; Accepted 16 February 2019
Available online 23 February 2019
0955-5986/

In the literature most of the studies were made in horizontal pipes [12–19], but the core-annular flow of two immiscible liquids with very different viscosities has been also proposed as an efficient and low cost method for producing heavy oils in vertical wells using water as a lubricant [3,20–22]. Nevertheless, there are few works focused on the measurement of water film thickness or dedicated to detailed film topological properties study and their relationship with the hydrodynamic stability of the core-annular flow [10,12,23,24].

1.2. Dispersed oil-in-water flow (reverse emulsion)

Dispersed oil-in-water flow pattern, where the oil is dispersed as droplets into the water-dominated flow, occurs in liquid-liquid pipe flow at high superficial velocities. This pattern is common in crude oil production and offshore pipelines [25]. However, it has not been studied as intensively as separated or intermittent flows. The drag reduction phenomenon in an interesting feature of this two-phase flow pattern, where the pressure drop reaches values even lower than those observed in single-phase water flow. For instance, a pressure-drop reduction of up to 25% in a viscous oil-water dispersed flow has been recently reported [5]. Drag reduction occurrence without the addition of any drag-reduction agent in dispersed flow has been reported in some works [5,26–31], but it has not been well understood yet.

In a literature review on experimental studies in oil-in-water dispersed flow in pipes, it is clear that low-viscosity oils were used in most of the works [28–30,32–37]. Differential pressure transducers [5], quick-closing valves and video cameras [5,38,39] were the main instrumentation. In a few cases, impedance sensors [29,30,35,37] and gamma-ray densitometers were used [36,40]. Studies relating the liquid film characteristics, i.e. amplitude and frequency of interfacial waves, with the drag-reduction phenomenon were not found.

The main objective of this work is to verify experimentally the presence of the water film theorized by Rodriguez et al. [5] in fully dispersed oil-in-water flow and quantify its geometrical and kinematic characteristics. The observed water-film region, near the pipe wall, is not a region completely free from oil drops, because an oil droplet may eventually be seen near the pipe wall. Nevertheless, according to Ref. [5], the oil droplets are always repelled towards the pipe core. In this work, it was assumed that there is a stable water film near the wall in fully dispersed oil-in-water flow, with a characteristic space and time-averaged thickness. This pragmatic model is chosen since it allows the measurement of time and space-averaged water-film thickness with simplicity through both optical and electrical-impedance techniques.

Only a few measurement techniques for liquid-liquid flows have been proposed [41]. Depending on the specific application it is more suitable to use one or another. For example, a high temporal resolution (greater than 5000 frames per second) is desirable for oil-in-water dispersed flow, where the mixture velocity is very high, whereas high spatial resolution is essential for measuring the topology of high-frequency waves in core-annular annular flow. The capacitive planar sensor that is being proposed in this work has the advantage of having a broader film-thickness range of measurement and the flexibility of application on separated and dispersed flow patterns.

This paper is divided into five sections, including this introduction. In Section 2 features of the experimental setup and test fluids are presented. Following, the proposed measurement system and the experimental procedures are detailed in Section 3. In Sections 4 and 5 the experimental results and conclusions are presented, respectively.

2. Materials and methods

The experimental work was performed at the Multiphase-Flow-Loop Test Facility of LETeF (Thermal-Fluids Engineering Laboratory), the Engineering School of São Carlos of the University of São Paulo, where simultaneous oil, water and air flow can be produced. A schematic view of the facilities is shown in Fig. 1 and Table 1 lists the main instruments and equipment.

The experiments were made in a vertical test section formed by a 12-m-height glass pipe of 50.8 mm, water and oil pumps (BW and BO, respectively) and instrumentation as flow rate meters, quick-closing-valves, etc. The fluids used in the experiments were a refined mineral oil and tap water. Oil and water physical properties are listed in Table 2. The electrical characteristics of the fluids were measured with an impedance analyzer Solartron 1260 at frequency of 5 MHz with an accuracy of 0.1%.

The flow patterns were recorded and identified via visualization technique using a high-speed video camera Olympus i-Speed3, at 5000 fps. The camera was placed in front of the pipeline, at 6.75 m from the entrance of the fluids. The high-speed camera was synchronized with the proposed measuring system. The camera configuration used in the experiments can be seen in Table 3.

The optical distortions (parallax and lens effects) due to the pipe wall were minimized using a solid acrylic box designed and constructed as an independent piece and then installed in the horizontal pipeline, Fig. 2. For the lighting system, two LED lamps of 30W and 2300 lumen were used.

2.1. Test matrix

The experimental regions were restricted to the green areas on the flow pattern map of Bannwart et al. [8], Fig. 3. Because, as mentioned before, studying dispersed oil-in-water and annular flows (core-annular flow) is the interest of this work. The water superficial velocity varied between 0.1 m/s and 0.3 m/s for annular flow and between 0.7 m/s and 1.96 m/s for dispersed oil-in-water flow. The oil superficial velocity varied between 0.3 m/s and 0.8 m/s for both cases. The experimental points were chosen such that the water film thickness could be measured with the capacitive system, i.e., when the film thickness was less than 2200 μm.

3. Capacitance liquid-film-thickness measurement system

The proposed liquid-film thickness measurement system consists of seven parts, Fig. 4. The waveform generator, the analog-digital converter (ADC) and the Field Programmable Gate Array (FPGA) are integrated through a National Instrument PXI-1072 equipment [42]. The transmitter and receiver circuits were designed and assembled during this work and they are based on the circuits used in the capacitance Wire-Mesh sensor [43]. The capacitance technique was chosen, over the conductance one, because even after an oil drop sticks on the wall, the isolating oil film does not affect the measurement; at least for low viscosity oils. The sensor used in this investigation was developed in LKE Lab, ETH Zurich. The FPGA controls the system by producing synchronized signals to activate each transmitter and the high-speed camera. The analog multiplexer sources the signal to the transmitter electrodes (Tx) in the planar sensor. The amplifiers give a proportional signal to the capacitance of the fluids over each pair transmitter-receiver (Tx-Rx). The ADC converts the measured signal in a digital signal and that signals are storage in the computer.

The system can be characterized by: (i) a spatial resolution of 4 × 4 mm^2 (one pixel in the resulting frame represents a square area with that size), (ii) a depth resolution of 6.2 μm, calculated by measuring the maximum and minimum voltages and taking into account the ADC resolution, i.e., it is possible to differentiate changes in the film height of 6.2 μm and (iii) a temporal resolution of 200 μs (one frame time), which depends on the time for reaching a steady-state signal in the transmitter. Consequently, the waves or fluid structures near to the pipe wall could have a maximum velocity of $V_{max} = 3$ m/s. The measurement range of the measurement system is from 400 μm to 2200 μm.

A schematic view of the circuit used in the system is showed in Fig. 5. The measurement system is supplied by a sinusoidal signal. The system has 208 measuring points, each row is activated (each Tx)

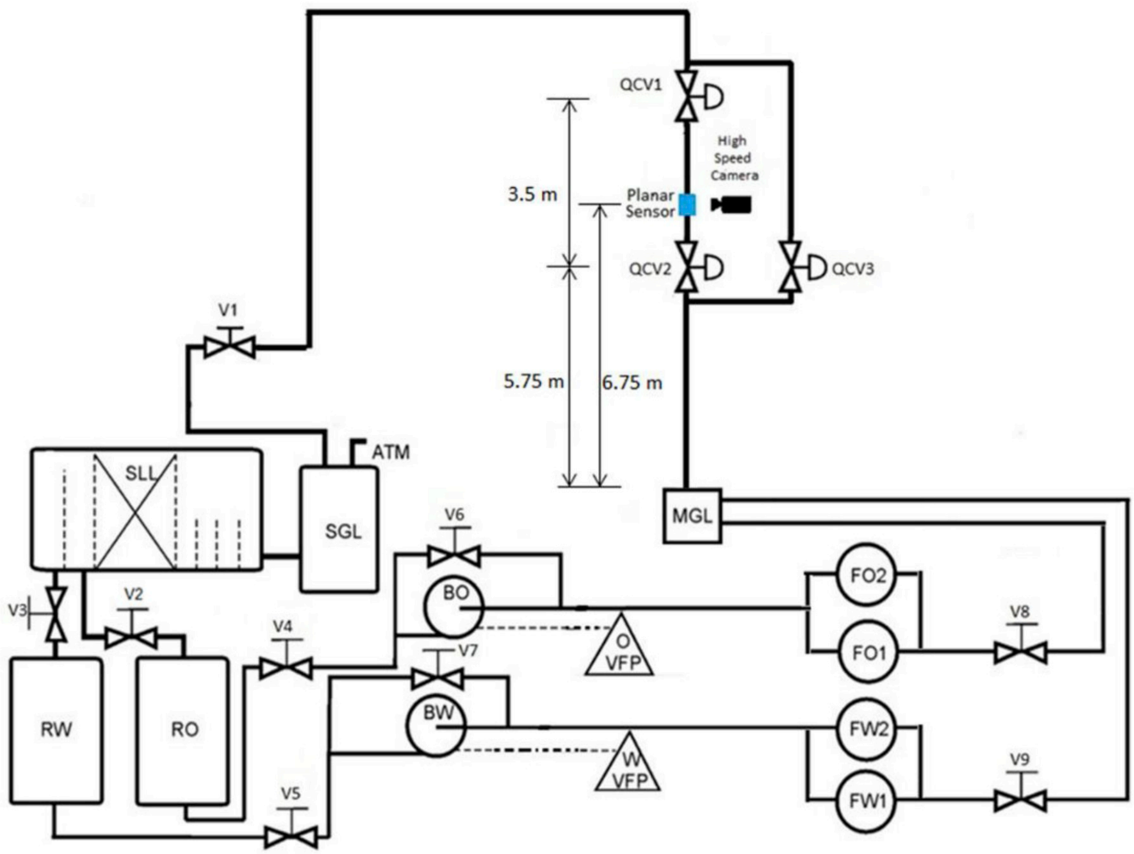

Fig. 1. Schematic of the experimental multiphase flow facility at LETeF.

Table 1
Main instruments and equipment of the facility.

Symbol	Description	Symbol	Description
	W VFP – Water Variable-frequency driver O VFP – Oil Variable-frequency driver		FO1, FO2– Oil Flow Meters FW1, FW2 – Water Flow Meters
	QCV1, QCV2, QCV3 - Quick Closing Valve		Control Valve
TDP	Differential Pressure Transducer		BW – Water Pump BO – Oil Pump
SLL	Coalescent-plates liquid-liquid separator	RW	Water Tank
MGL	Multiphase mixer	SGL	Gas-liquid separator Tank
RO	Oil Tank		

Table 2
Characteristics of the fluids.

Fluid	Viscosity (cP at 25°)	Density (kg/m^3)	Relative Permittivity (−)	Conductivity (S/m)
Water	1	988	79	4.12×10^{-3}
Oil	220	860	3.5	0.04×10^{-15}

sequentially by the analog multiplexer. There are 16 transimpedance amplifiers and 16 logarithmic amplifiers. The used ADC has 16 simultaneous channels.

3.1. Planar sensor

A planar sensor is a sensor where the electrodes are placed in a coplanar plane. Two important advantages of these kind of sensors are: only a single-side access to the test material is required and the strength of the output signal can be controlled by changing the area of the sensor, the number of electrodes or the spacing between them.

Table 3
Camera configuration.

Feature	Value
Resolution	804 × 600 pixels
Frames per second	5000
Shutter	190 µs
Trigger mode	ROC (Record on Command)
Trigger event	Falling
Lens	AF-S Micro Nikkor 60 mm f/2.8D

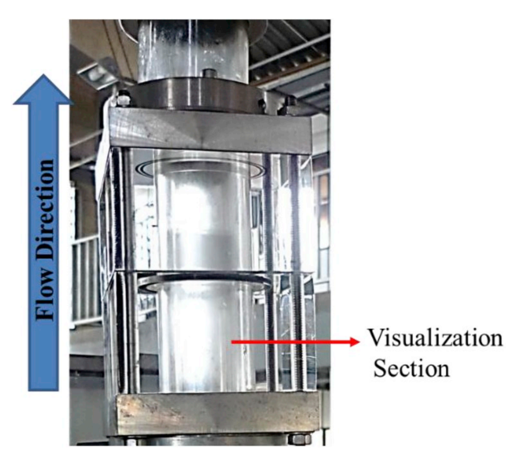

Fig. 2. Detail of visualization section.

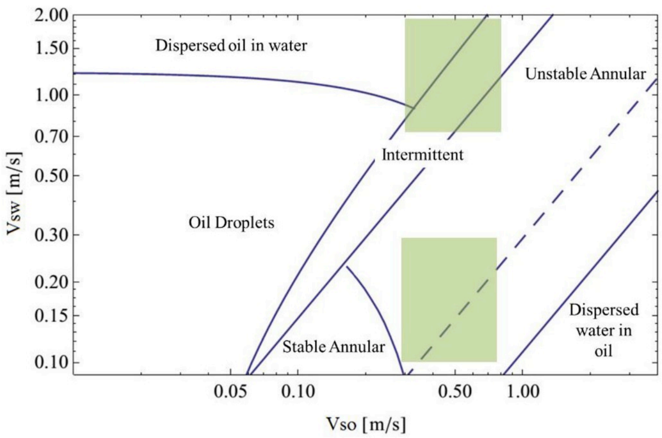

Fig. 3. Flow map of superficial velocities, upward-vertical oil-water flow in 50.8-mm i.d. pipe, based on [8].

The planar sensor used in this work has three types of electrodes: transmitters (Tx), receivers (Rx) and ground. The sensor is arranged in a two-dimensional array, where the transmitters are connected in one direction (transmitter lines), while the receivers are placed perpendicular to this direction (receiver lines). It was manufactured using multilayer printed circuit board (PCB) fabrication technology and flexible material; some of the sensor characteristics are summarized in Table 4.

The sensor has a total sensing area of 192 (length) × 52 (width) mm^2, Fig. 6. It consists of 5221 electrodes with diameters of 0.9 mm and 5220 electrodes with diameters of 0.5 mm (Fig. 7). In Fig. 5, there is an example where Tx2 is active; the blue square highlighted over the sensor represents the sensing area of the pair Tx2-Rx2. The spatial resolution is the region of measuring of a pair Tx-Rx (the blue region in Fig. 5), which corresponds to the spatial separation between electrodes, which is 4 × 4 mm^2. The electrodes are the only conductive portion of the sensor in contact with the fluids. The sensor is detailed in Ref. [44].

It is possible to obtain three different combinations of receiver and transmitter electrodes. The different arrangements possible of sensors in the planar sensor (matrix) are summarized in Table 5. Each matrix corresponds to a set of pair Tx-Rx with the same spatial resolution. The matrix with spatial resolution of 4 × 4 mm^2 was selected according to the expected film thickness in this work given by preliminary experiments using high-speed camera. Although the sensor is able to work with more receivers, only 16 receivers were used, because the analog-digital converter stage had 16 analog inputs, resulting in an effective sensing area of 192 mm × 52 mm, as marked in Fig. 6.

3.2. Receiver circuit

The receivers are connected to auto-balancing bridges (Fig. 8) where the fluids over the electrodes have an impedance represented by C_x and G_x. At low frequencies (f < 100 MHz), the admittance of a fluid can be modeled as a conductance (G_x) in parallel with a capacitance (C_x) [45]. The conductance is $G_x = k_g \sigma_x$ and the capacitance is $C_x = k_g \varepsilon_0 \varepsilon_x$, where k_g is a variable associated to the electrodes shape and the film thickness, σ_x is the equivalent conductivity, ε_0 is the vacuum permittivity (8.85 pF/m) and ε_x is equivalent relative permittivity. Assuming that the equivalent conductivity and permittivity are dominated by the water values (σ_w = 0.00412 S/m and ε_w = 80), the gain of the auto-balancing bridge will be

$$\frac{U_{out}}{U_{in}} = -\frac{k_g(\sigma_w + j2\pi f \varepsilon_0 \varepsilon_w)}{G_f + j2\pi f C_f}. \tag{1}$$

At the work frequency of 5 MHz, the denominator of Eq. (1) is approximately equal to $j2\pi f C_f$ and the numerator is $k_g(0.00412 + j0.0222)$ S/m. Thus, the capacitive part contribution is 84.4%. Therefore, the circuit is dominated by the capacitive component. This approach is enough for practical purposes.

The output of the circuit is proportional to the fluids' capacitance over the pair Tx-Rx,

$$U_x = A \ln(U_{out}) + B \tag{2}$$

where

$$U_{out} = -\frac{C_x}{C_f} U_{in} \tag{3}$$

and A and B depend on the geometric parameters and circuit parameters. Given that the geometric parameters change during the measurements, A and B cannot be estimated for all the cases. Instead, to solve Eq. (2), an empirical approximation is used to correlate the film thickness (δ) with U_x. The empirical relation is found through a calibration process proposed by Damsohn in Ref. [44], and detailed in the next section. Known water-film thicknesses are located over the sensor and the output voltage is recorded, for each thickness. Therefore, it is possible to obtain an equation relating the water-film thickness and the output voltage.

In order to minimize the variation in the circuit parameters and the possible deposition of oil on the sensor surface, a measurement of voltage with the system saturated (U_{sat}, i.e. the sensor covered with water with a bigger thickness than the saturation thickness) is made during the process of calibration and before and after each experimental run in the pipeline. Thus, the dimensionless voltage (U_{dl}) is defined as

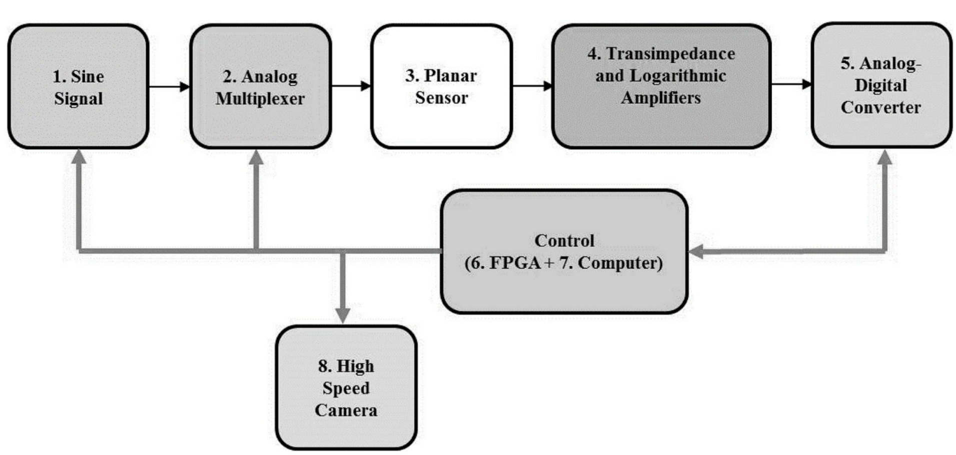

Fig. 4. Schematic diagram of the information flow for the proposed liquid-film thickness measurement system.

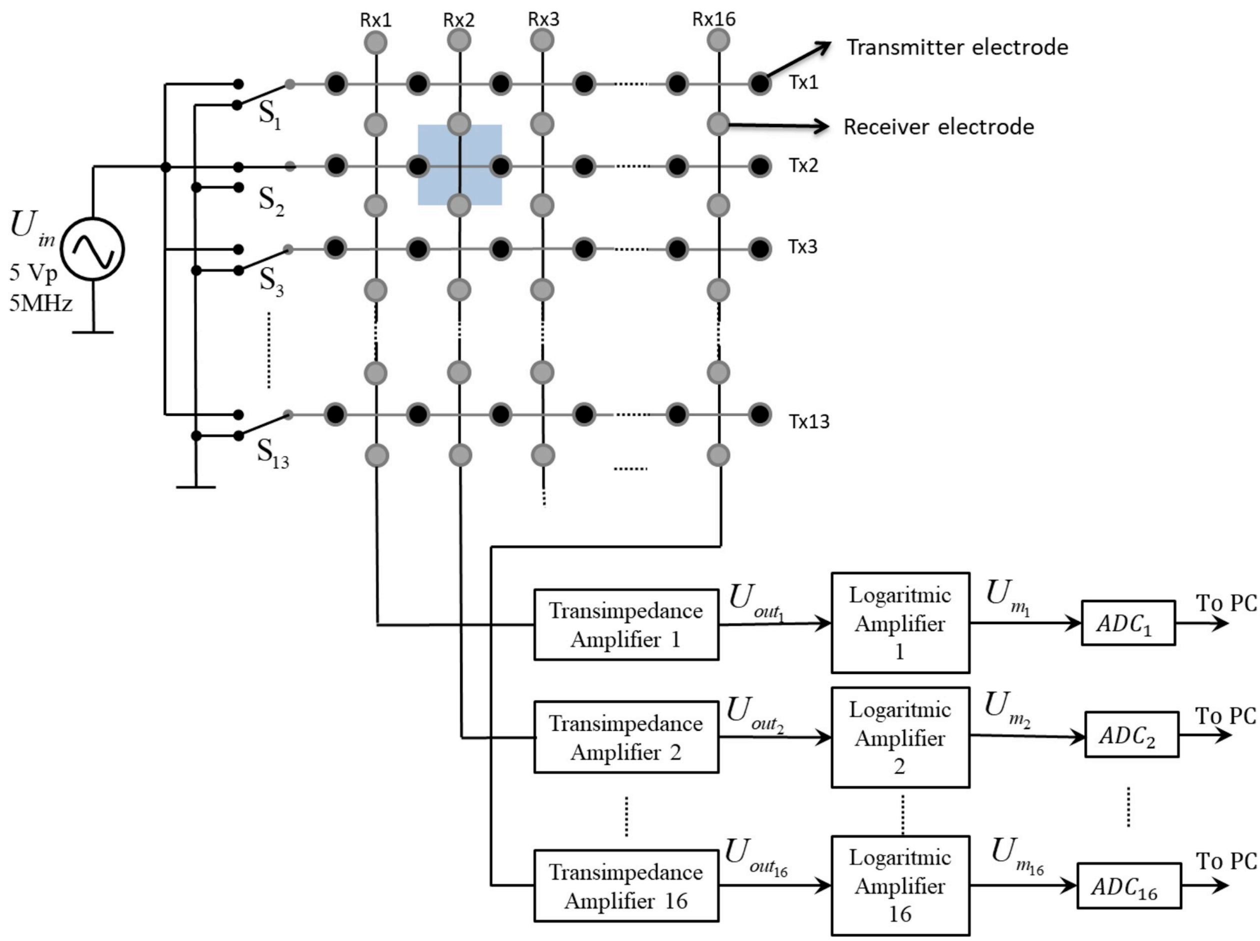

Fig. 5. Schematic view of the circuit used in the proposed liquid-film thickness system.

Table 4
Characteristics of the planar sensor.

Feature	Value
PCB material	Polyimide
Conductive material	Cooper
Coating material	Gold (to prevent corrosion)
Coating layer size/Number of layers	5 µm/9
Laser-drilled holes diameter	0.25 mm
Path sizes	0.1 mm
Space between insulating and electrodes	20 µm
Mean sensing area thickness	0.40 mm

$$U_{dl} = \frac{U_x}{U_{sat}}. \quad (4)$$

4. Results and discussion

One of the main goals of this research is to assess the capability of the proposed capacitive planar-sensor system for measuring a thin water film thickness in oil-water flow. The observed annular flow is mainly characterized by an oil core surrounded by a water film but drops of several different sizes and shapes can be observed flowing dispersed in the latter. In fully dispersed oil-in-water flow a concentration of water in the region adjacent to the pipe wall has been identified recently [28]. A total of 44 oil-water experiments (33 annular and 11 dispersed) were carried out. The film thickness was recorded at 5000 frames/second for one second with synchronized capacitance planar sensor and high-speed video camera.

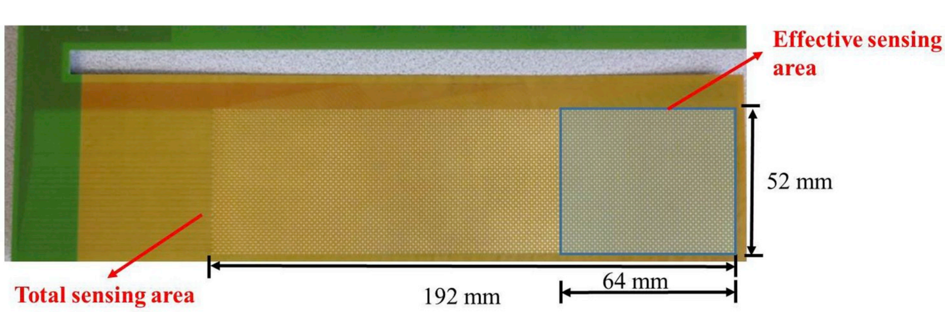

Fig. 6. General view of the planar sensor used in this work.

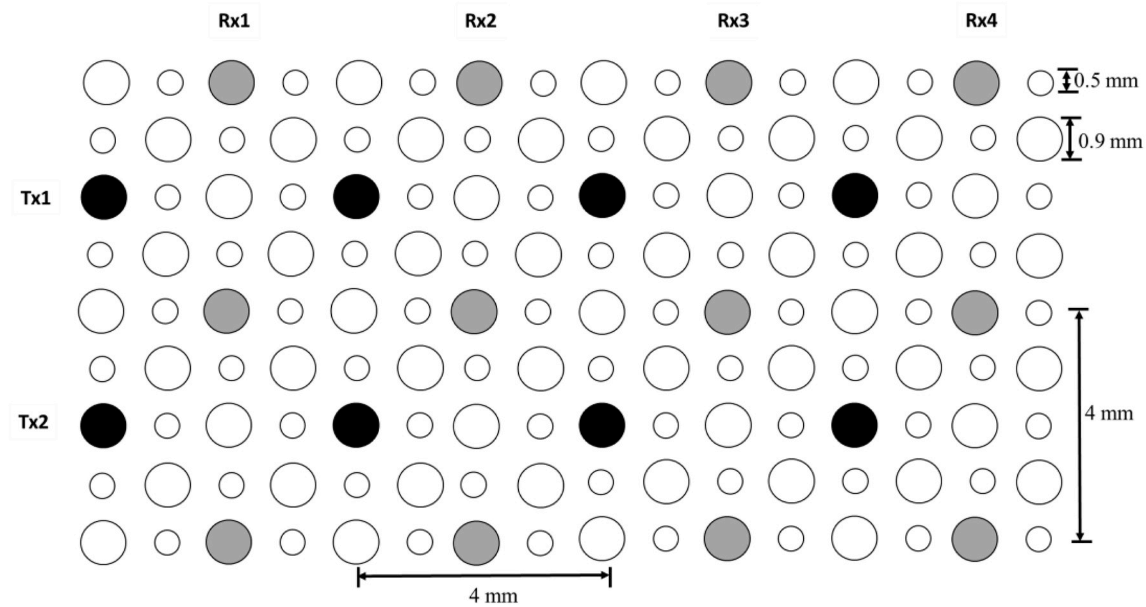

Fig. 7. Detailed view of the planar sensor where the black circles are the transmitter electrodes and the gray circles are the receiver electrodes.

Table 5
Characteristics of each matrix of the planar sensor.

Matrix	Number of Tx	Number of Rx	Spatial Resolution	Measurement range
Near field	26	96	$2 \times 2\,mm^2$	100 µm–700 µm
Middle field	13	48	$4 \times 4\,mm^2$	400 µm to 2200 µm[a]
Far field	9	32	$12 \times 12\,mm^2$	1000 µm–3500 µm

[a] Measured values using the proposed capacitance system.

4.1. Calibration

A calibration is necessary in order to correlate the signal obtained from the receiver electrodes to the film thickness. During the calibration in this work, the sensor was inclined at an angle of 45° and immersed into water. After, different cylinders with spool shape and known gaps were rolled over the sensor. The measured value is the minimum measured value, when the cylinder is passing over the measuring point [44]. Fig. 9 shows the calibration elements; one can see the calibration box, where the sensor was fixed and maintained straight, and some of the cylinders used in the tests.

The calibration was made using eighteen cylinders made of polyvinyl chloride, PVC, with a relative permittivity of 3 (identical to the oil relative permittivity). These cylinders have gaps (δ) between zero and 2400 µm. Each cylinder was rolled over the sensor ten times. The film thickness, δ, in each measurement point was be calculated as

$$\delta = a_1 U_{dl}^4 + a_2 U_{dl}^3 + a_3 U_{dl}^2 + a_4 U_{dl} + a_5 \quad (5)$$

where a_1 to a_5 are the polynomial coefficients determined by the calibration curve fitting and U_{dl} is calculated by eq. (4).

4.2. Uncertainty analysis

Three error sources were taken into account to compute the uncertainty of the film thickness measurement system presented in this work. First, the gap measurement in the calibration cylinders (calibration error). Second, the deviation from the calibration curve. Finally, statistical variations of the measured values (data acquisition system error).

The film thickness measurement system uncertainty for all the measurement range, taking Tx5-Rx5 as reference, is

$$\pm 85\,\mu m < u_{system} < \pm 105\,\mu m. \quad (6)$$

The first bound is related to water film thickness of 100 µm and the second is related to the larger measured film thickness (2200 µm). More details about the uncertainty analysis can be seen in the Appendix at the end of the paper.

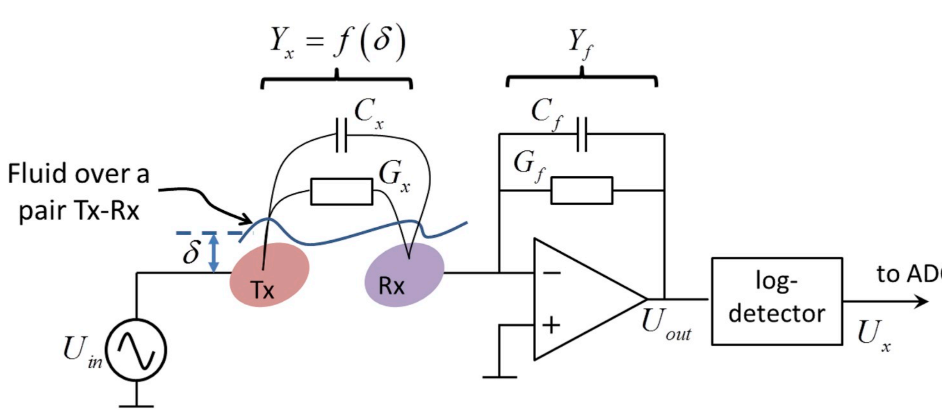

Fig. 8. Reception circuit schematic.

Fig. 9. Calibration elements. a) Calibration box and b) Sample of cylinders.

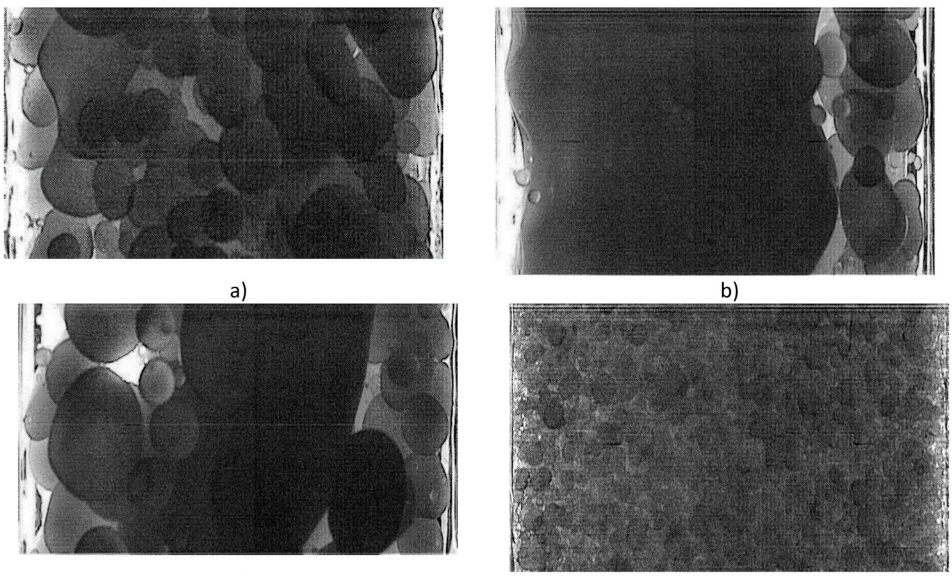

Fig. 10. Observed flow patterns where the dark drops are oil. a) big drops (V_{so} = 0.4 m/s and V_{sw} = 0.2), b) unstable annular (V_{so} = 0.3742 m/s and V_{sw} = 0.15), c) unstable annular (V_{so} = 0.3 m/s and V_{sw} = 0.1 m/s) and d) dispersed oil-in-water (V_{so} = 0.5 m/s and V_{sw} = 1.5 m/s).

4.3. Observed flow patterns

The three different oil-water flow patterns observed can be seen in Fig. 7: “big drops” (Fig. 10a), “unstable annular” with dispersed drops (Fig. 10b and c) and “dispersed oil-in-water” (Fig. 10d). One can see in Fig. 11 the observed flow regimes on an oil-water flow map for vertical pipes. These experimental points were chosen such that the water film thickness could be measured with the capacitive system. The transition boundary between dispersed oil-in-water flow and unstable annular corresponds to the theoretical one (Fig. 3).

The observed two-phase flow patterns can be classified as water-dominated flow patterns, where water is the continuous phase [46]. In big-drops flow (Fig. 10a), oil was arranged as globules, with medium and large sizes, traveling in the water-dominated region. In unstable annular flow, it was possible to distinguish two kind of oil structures flowing (Fig. 10b and c). In the first (Fig. 10b), there was a core oil body with an irregular shape (worm like) and in the second (Fig. 10c) core elongated drops or slugs surrounded by different size oil drops. At last, dispersed oil-in-water (Fig. 10d) was characterized by droplets, mostly with spherical shape, flowing very close to each other.

4.4. Water film thickness

The planar sensor was made of a flexible material that allowed it to be taped to the internal wall of the tube, Fig. 12a. A suitable part was designed and manufactured to place the sensor between two sections of the pipe, which included a downstream visualization section. In Figs. 6 and 12b it can be seen that the sensor sensing area (52 mm × 64 mm), 52 mm in the axial direction x 64 mm in the circumferential direction (along the pipe wall curvature). The green line refers to a line of transmitters (Tx) for a constant receiver and the red line refers to a line of receivers (Rx) for a constant transmitter.

The axial water-film thickness distribution over a line of transmitters (Tx) for a constant receiver, i.e. the thirteen transmitters (Tx1 to Tx13) were excited one by one and the signal obtained in the receiver Rx2 was recorded (refer to Fig. 5), is showed in Fig. 13a for unstable annular flow and in Fig. 13c for dispersed oil-in-water flow. The circumferential water-film distribution over a line of receivers (Rx) for a constant transmitter, i.e. the transmitter two (Tx2) was activated and the signal in each receiver (Rx1 to Rx16) was recorded (Fig. 5), at a given instant of time is showed in Fig. 13b for unstable annular flow and Fig. 10d for dispersed oil-in-water flow.

It was possible to recognize similar behaviors in experiments in the same flow regime. On the one hand, unstable annular flow can be described by big oscillations in the measured film thickness in both flow direction (axial) and circumferential direction; the film thickness varies from 400 μm to 1800 μm in the axial direction and from 400 μm to 2200 μm in the circumferential direction. The big fluctuations are

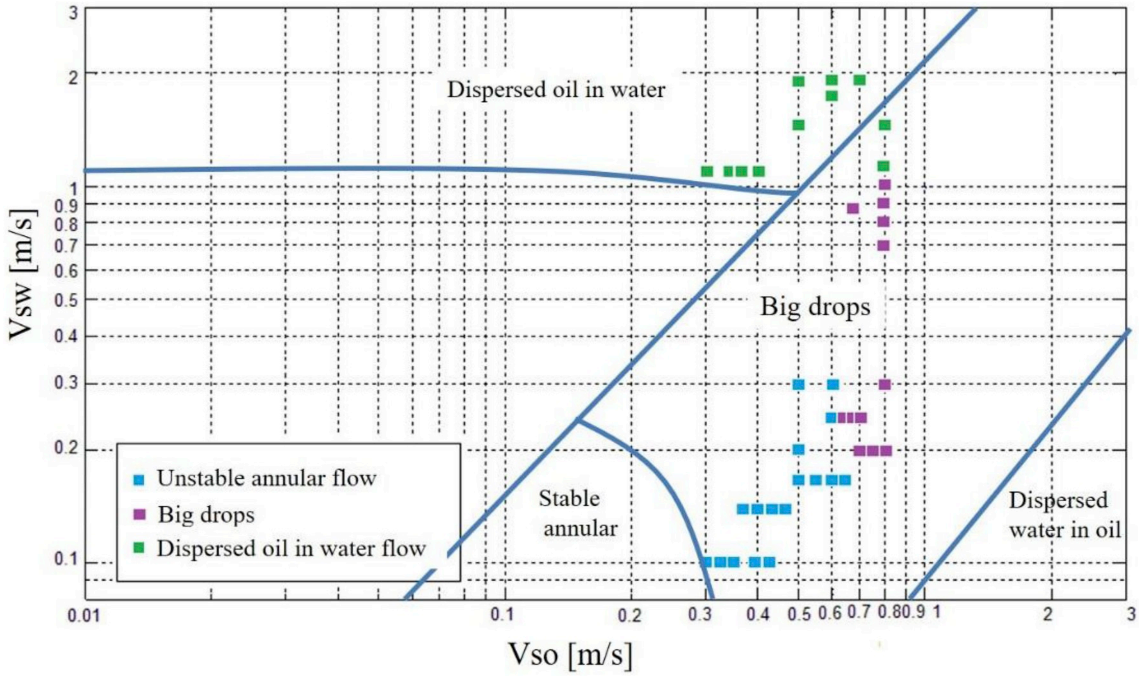

Fig. 11. Observed flow patterns as function of oil superficial velocities and water superficial velocities.

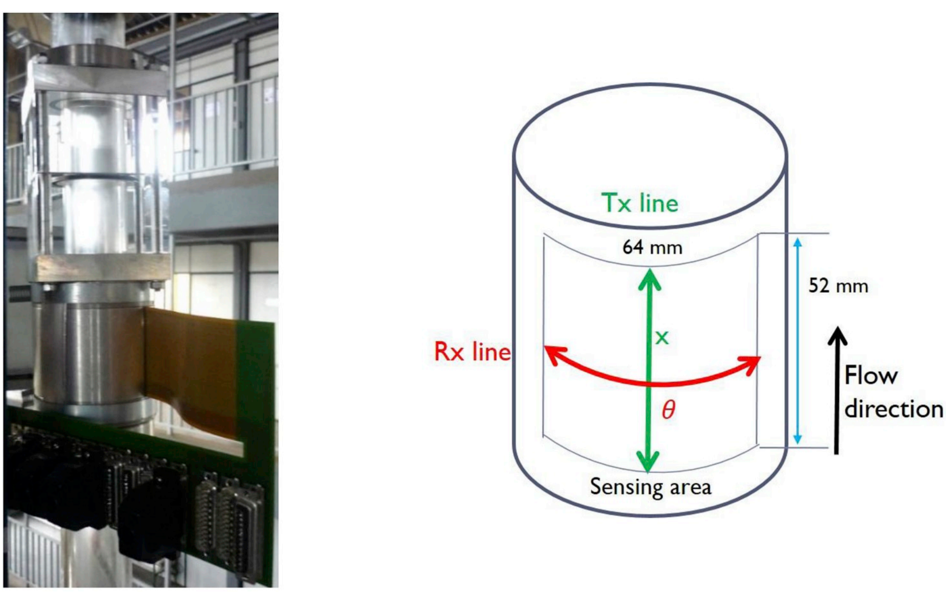

a) b)

Fig. 12. a) Photo of the entire system and the visualization section placed in the pipeline, b) film thickness for all the Tx and one Rx in green (along the pipe) and film thickness for all the Rx and one Tx in red (pipe perimeter). (For interpretation of the references to colour in this figure legend, the reader is referred to the Web version of this article.)

related to big interfacial structures flow i.e. oil drops and the unstable oil core (Fig. 13a and b). On the other hand, in oil-in-water dispersed flow the fluctuations are less intense, in general the measured film thickness was fluctuating from 900 μm to 1900 μm in the axial direction and from 1400 μm to 2200 μm in the circumferential direction. In dispersed oil-in-water flow the sensor is not registering a proper film, but a concentration of water fraction near the pipe wall. These results are consistent with the occurrence of smaller interfacial structures as the observed oil droplets dispersion. The signal agrees to a more uniform oil-droplet distribution (Fig. 13c and d). This technique could be scaling up to full size well-bore. The maximum thickness to be measured is defined by the size and separation between electrodes. Bonilla et al. [47] compare several sensor geometries to the be applied in a viscous oil–water flow. In general, to increase the penetration depth must be increased these dimensions.

One can see in Fig. 14 the time signal of a given measuring point (one transmitter – one receiver) during 0.02 s (100 samples) for two experiments in unstable annular flow regime (Fig. 14a) and two experiments in dispersed oil-in-water flow regime (Fig. 14b). As observed in Fig. 14, the unstable annular flow signals have larger amplitudes (from 400 to 2000 μm) when compared with the signals related to dispersed flow (from 800 to 2000 μm). The results suggest that there is a higher concentration of water fraction near the pipe wall in dispersed oil-in-water flow in comparison with unstable annular flow. For the experiments illustrated in Fig. 14, the average film thickness in unstable annular flow (Fig. 14a) is 809 μm (V_{sw} = 0.15 m/s and V_{so} = 0.37 m/s) and 732 μm (V_{sw} = 0.15 m/s and V_{so} = 0.4 m/s), whereas the average equivalent water layer in dispersed oil-in-water flow (Fig. 14b) is

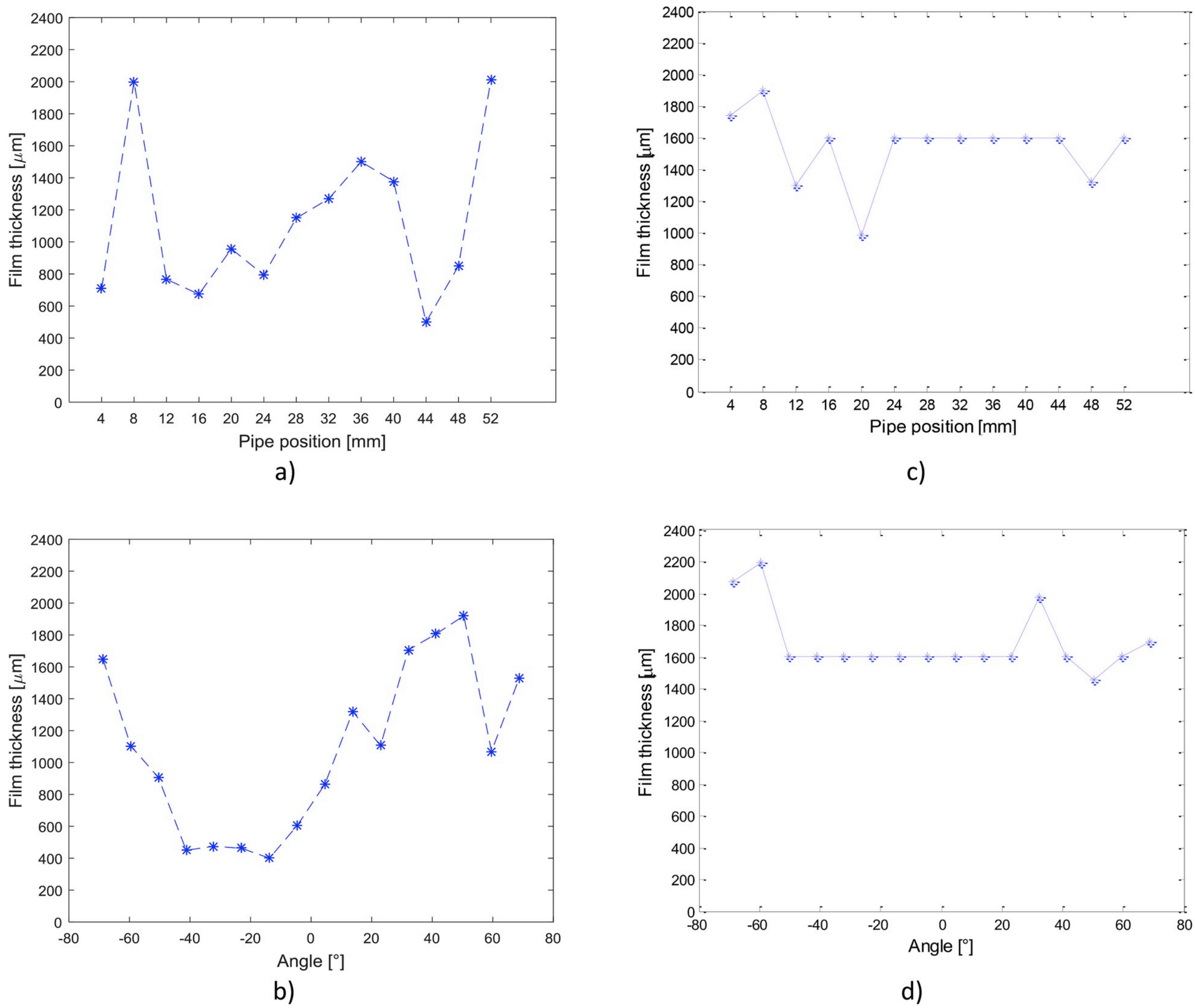

Fig. 13. Signal obtained with the planar-sensor system for unstable annular flow (left images) at $V_{sw} = 0.15$ m/s and $V_{so} = 0.4$ m/s and dispersed oil-in-water flow (right images) at $V_{sw} = 1.7$ m/s and $V_{so} = 0.6$ m/s; a) and c) film thickness over an axial line of transmitters (Tx) for a constant receiver (along the pipe); b) and d) film thickness over a circumferential line of receivers (Rx) for a constant transmitter (pipe perimeter).

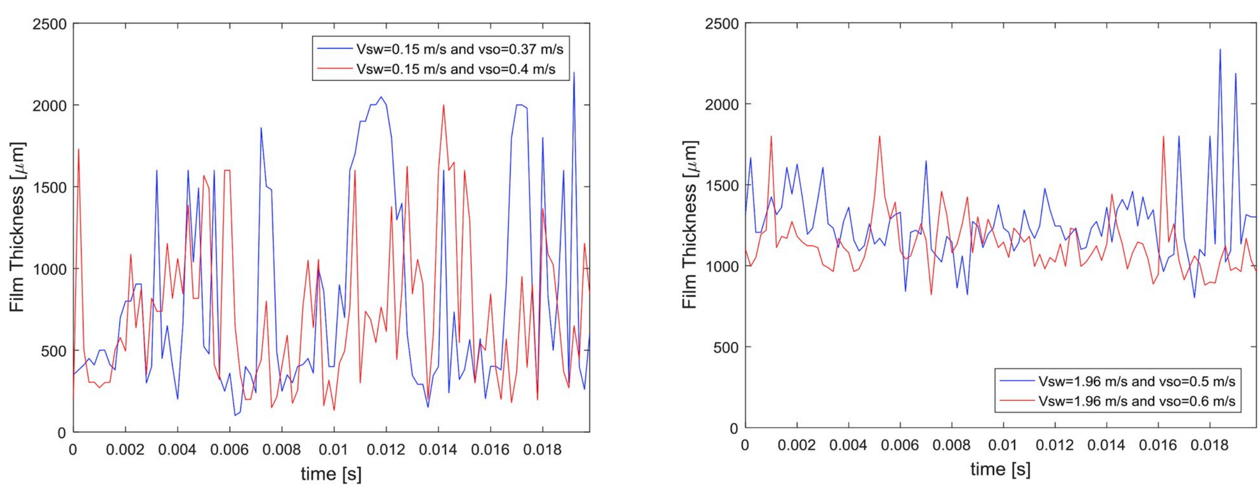

Fig. 14. Measurements at a given measuring point as a function of time for four experiments. a) Unstable annular flow, in blue $V_{sw} = 0.15$ m/s and $V_{so} = 0.37$ m/s, in red $V_{sw} = 0.15$ m/s and $V_{so} = 0.4$ m/s. b) Dispersed oil-in-water flow, in blue $V_{sw} = 1.96$ m/s and $V_{so} = 0.5$ m/s, in red $V_{sw} = 1.96$ m/s and $V_{so} = 0.6$ m/s. (For interpretation of the references to colour in this figure legend, the reader is referred to the Web version of this article.)

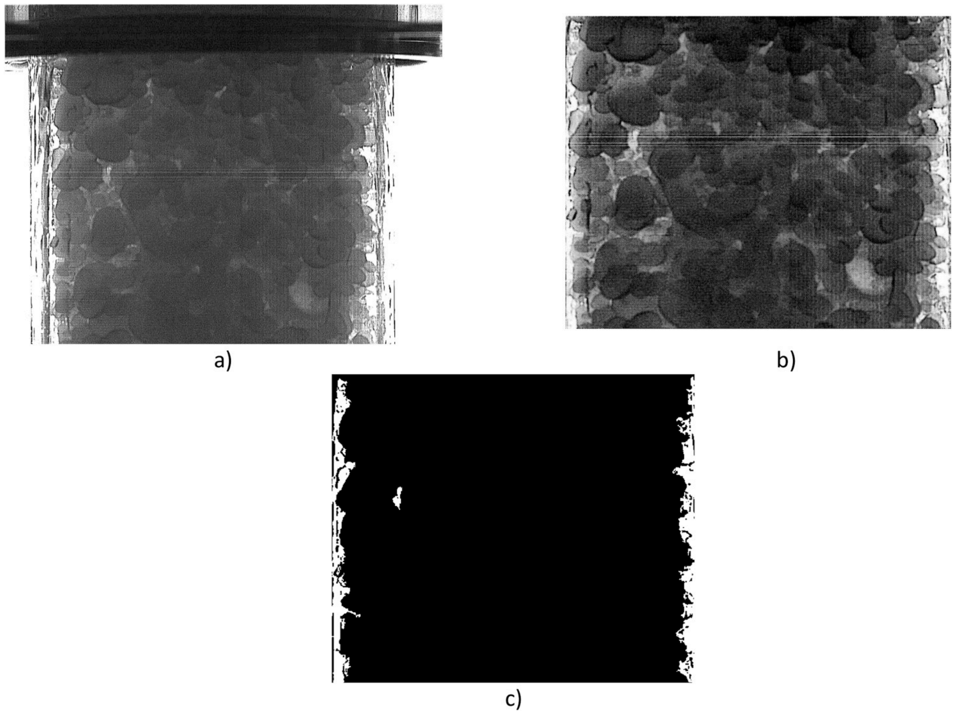

Fig. 15. Image processing results; a) original snapshot, b) pre-processing and c) segmentation result (V_{so} = 0.8 m/s and V_{sw} = 0.8 m/s experiment).

1790 µm (V_{sw} = 1.96 m/s and V_{so} = 0.5 m/s) and 1717 µm (V_{sw} = 1.96 m/s and V_{so} = 0.6 m/s).

The water-film-thickness data obtained by the planar sensor were compared with those obtained by camera-based imaging technique. The high-speed video camera images were processed using the algorithms presented in Ref. [48]. First, the images were pre-processed. Next, the images were segmented. One can see in Fig. 15 an original snapshot, the resulting image after applying the pre-processing step and the result of the segmentation stage.

The segmented images are calibrated to find the relationship between pixel and length magnitudes, i.e., to determine what a pixel represents in terms of size or distance. The calibration was made using as square pattern with 0.2 mm × 0.2 mm squares. Since light enters the camera through a lens, images suffer from some optical distortion. A square (in the square pattern) near to the pipe wall is represented in an image by 3.3 pixels and by 4 pixels in the pipe center. Thus, the pixel scale factor (PSF) or pixel value obtained was 0.06 mm/pixel near to the pipe wall and 0.05 mm/pixel near to the pipe center.

Fig. 15c shows a segmented image where a black pixel represents oil and a white pixel represents water. The water film thickness is calculated from a segmented image multiplying each white pixel ($pixel_n$) by the corresponding PSF (PSF_n) and adding the results by rows.

$$\delta = \sum_{n=1}^{Np_w} pixel_n \times PSF_n, \tag{7}$$

where Np_w is the number of white pixels in a row.

The mean film thickness $\bar{\delta}$ for one frame is

$$\bar{\delta} = \frac{1}{Np}\sum_{i=1}^{Np}\delta_i \tag{8}$$

where Np is the number of measurement points (13 × 16 points for the capacitive measurement system and 668 columns for the images) and each pixel has a film thickness δ_i, calculated using eq. (5) for the proposed measurement system and eq. (7) for the high-speed-camera images technique.

The mean film thickness for each experiment was obtained by averaging 5000 frames, in both high-speed-camera images and capacitive technique. The mean film thickness for an experiment is calculated as

$$\bar{\delta}_{Exp} = \frac{1}{N_{frames}}\sum_{1}^{N_{frames}}\bar{\delta} \tag{9}$$

where N_{frames} is 5000 frames.

Snapshots taken with the high-speed camera and synchronized with the capacitive-measurement system are presented in Fig. 16 and Fig. 17, corresponding to unstable annular flow and to dispersed oil-in-water flow, respectively. A film thickness with zero value means oil touching the pipe wall. A capacitive system advantage is that it delivers a water-film topology 3D representation, instead of simple 2D projections. It is possible to observe that there are intense fluctuations in unstable annular flow along the flow direction (axial) as well as on the circumferential direction, but the fluctuations along the flow direction are slightly less intense than those over the perimeter direction (Fig. 16). An explanation is the shape of the oil drops, which is not spherical, but rather oval and oriented or stretched in the flow direction. The water flow dynamics (predominant shear stress in the flow direction) and interaction between droplets (viscous wake) are responsible for stretching the oil drops in the flow direction. The bigger the drops, the stronger the drop-stretching phenomenon, as interfacial-tension forces, which act to keep the drops spherical, become less important.

The fluctuations in dispersed oil-in-water flow are less intense and similar in both directions (Fig. 17). The intense turbulence that occurs in this flow pattern is responsible by the existence of smaller drops. The observed uniformity in the water-layer fluctuations can be explained by the existence of more spherical droplets; the smaller the drops, the stronger the interfacial-tension forces that try to keep them spherical. Therefore, homogeneous and isotropic fluctuations is expected, regardless the direction of observation.

The mean film thickness obtained by the capacitance system and the one obtained by the high-speed-camera image technique are compared for each experiment in Fig. 18, the dashed lines represent the values obtained using the high-speed-camera image technique and the deviation lines, different variations of those true values (+10%,-10% and

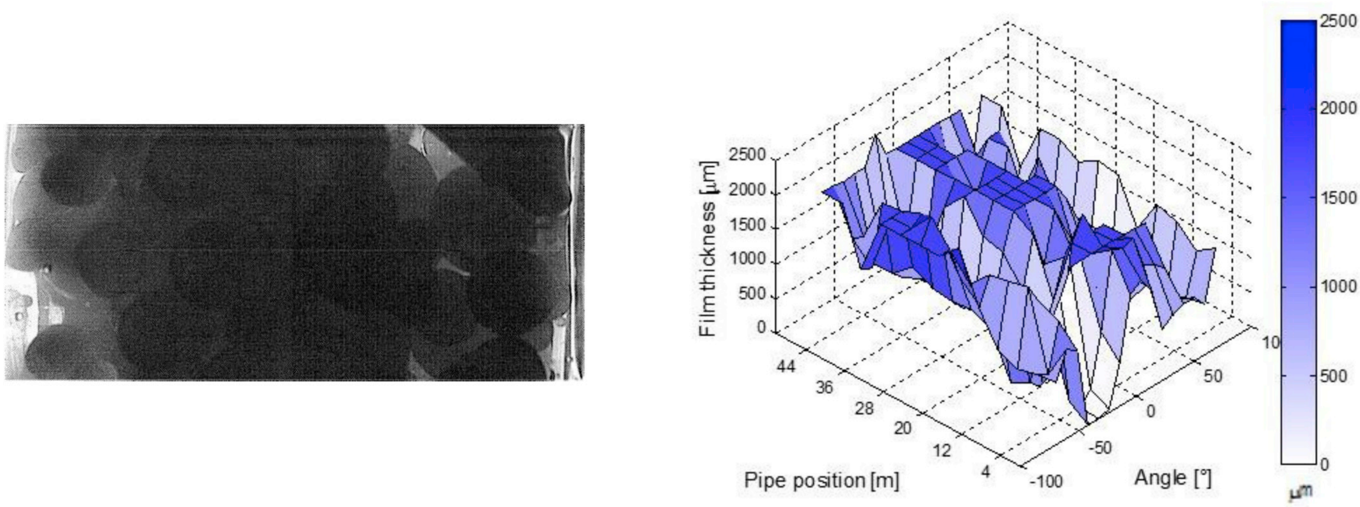

Fig. 16. Comparision of synchronized high-speed camera images (left) with measured 3D film thickness (right) in unstable annular flow (V_{sw} = 0.1 m/s and V_{so} = 0.35 m/s).

−20%). For the case of dispersed oil-in-water flow the term film thickness should be understood as water-layer thickness. The unstable annular and big drops flow patterns were analyzed as an unique flow pattern, called unstable annular flow, because there were oil drops with similar characteristics near to the pipe wall, which was the region of interest, as mentioned in section 4.3 and seen in Fig. 10.

The average relative error (*ARE*) was used to compare the two techniques, where ARE was calculated as:

$$ARE = \frac{\sum_1^N abs\left(\frac{\bar{\delta}_{camera} - \bar{\delta}_{system}}{\bar{\delta}_{camera}}\right)}{N} \times 100[\%], \tag{10}$$

where $\bar{\delta}_{camera}$ and $\bar{\delta}_{system}$ denote the measured film thickness with each technique. N is the number of experimental points.

The ARE is 12.4% and the deviation is −20% for unstable annular flow and 3.6% and −10% for dispersed flow, respectively. In Fig. 18 the black triangles are the capacitive system results having as reference the film thickness estimated using the image-technique. The experimental uncertainty using the camera-based imaging technique is 100 μm, corresponding to the half of the minimum scale of the square pattern used for calibration. As one can see in Fig. 18, the mean water film thickness ranged from 800 μm to 2100 μm for the unstable annular flow pattern and the water layer ranged from 1300 μm to 2200 μm for dispersed oil-in-water flow, respectively.

The camera-based imaging technique data overestimated the capacitance-system data, having a higher disagreement for the unstable-annular-flow case. The capacitive measurement system is able to record the water film thickness in different directions. It allows having 3D information about thickness variations, so one should expect to have a more refined and representative measurement of average film thickness than that provided by the camera-based imaging technique, which only records 2D projection of the film. The observed disagreement can be explained by inherent inaccuracies of the camera-based imaging technique, that may be overestimating the water film thickness value due to segmentation errors. During manual check-up procedures it was detected that some pixels related to oil drops presented gray values quite near to those chosen to represent the water phase. Some regions where oil drops were present could have been segmented as a continuous water phase. Therefore, optical distortions are probably the reason behind the observed disagreement.

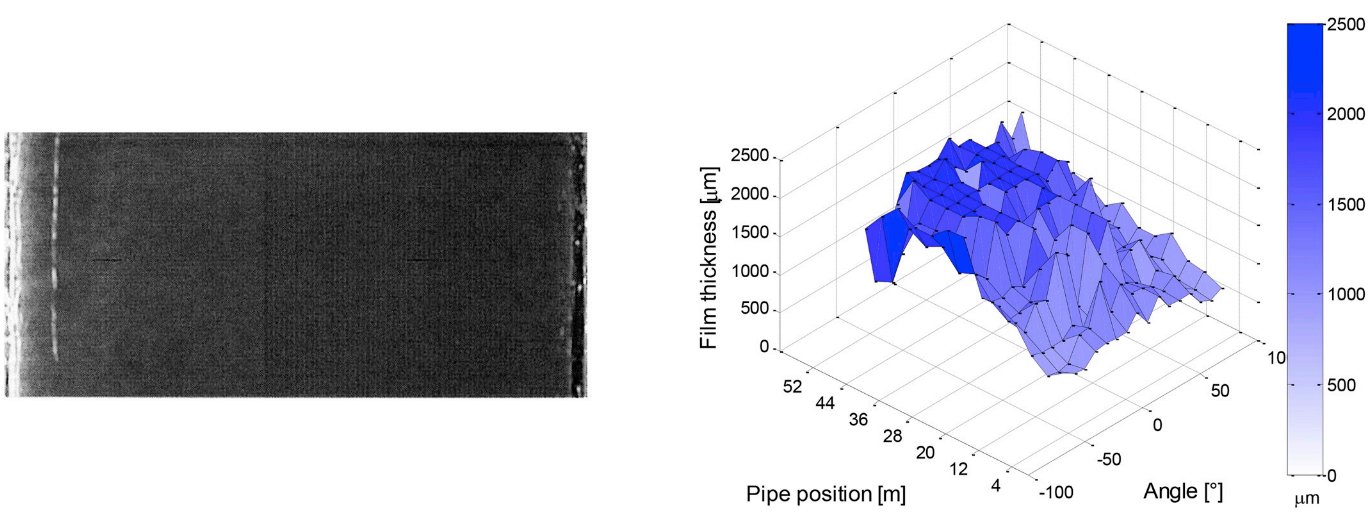

Fig. 17. Comparision of synchronized high-speed camera images (left) with measured 3D water layer thickness (right) in dispersed flow (V_{sw} = 1.2 m/s and V_{so} = 0.8 m/s).

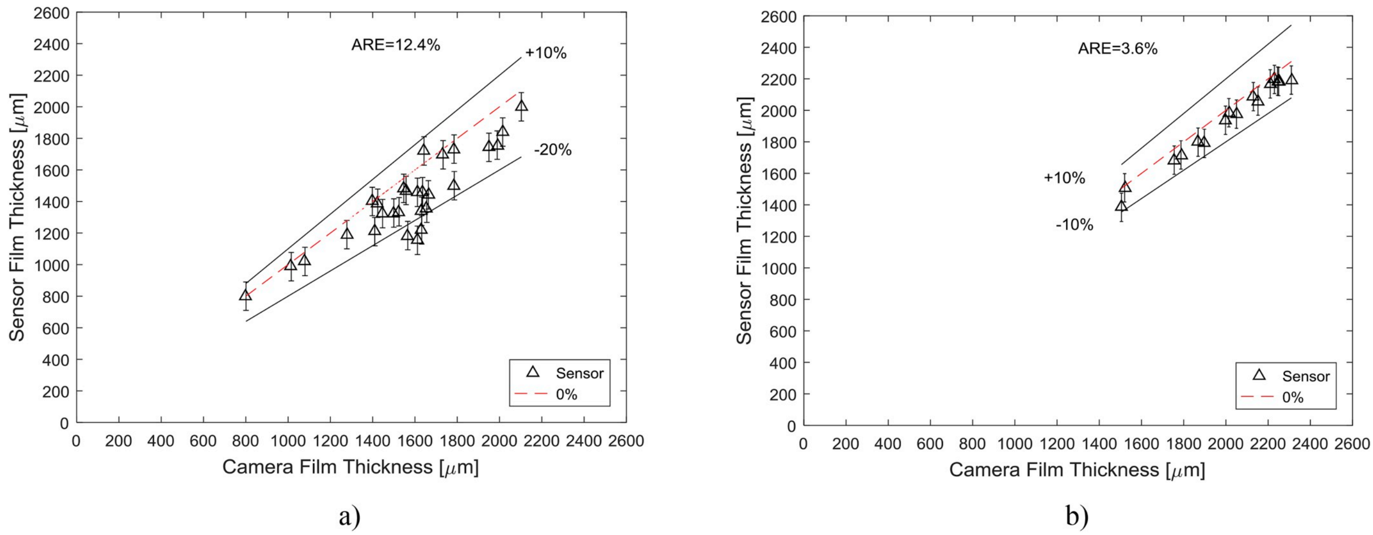

Fig. 18. Measured water film thickness using the proposed capacitance system; a) for unstable annular flow and b) for dispersed oil-in-water flow.

5. Conclusions

In this work it is proposed an invasive and non-intrusive water film thickness measurement system based on capacitance measurements for high-viscosity-oil-in-water flow. The system was used to study thin water films in unstable-annular flow and oil-in-water dispersed flow in a 12 m long vertical glass pipe, with 50.8 mm of inner diameter. The experiments were carried out at different water and oil superficial velocities (0.1–2.0 m/s and 0.3–0.8 m/s, respectively). These experimental points were chosen such that the water film thickness could be measured with the capacitive system. The system is composed by a planar sensor with spatial resolution of $4 \times 4\,mm^2$ and effective measuring area of 64 mm by 52 mm. The temporal resolution in all the experiments was 5000 frames per second.

In the cases studied in this work, the water film thickness ranged from 900 μm to 2100 μm for unstable annular flow and from 1300 μm to 2200 for dispersed flow. Unstable-annular flow was featured by big fluctuations related to the flow of big interfacial structures as oil drops and the unstable oil core, whereas in oil-in-water dispersed flow small fluctuations were observed, which were consistent with the observed smaller interfacial structures as oil droplets.

The average film thickness obtained by the capacitance system was compared with the one obtained by the camera-based imaging technique. It was found a relatively good agreement between the two techniques, the average relative errors were 12.4% and 3.6% for unstable-annular flow and for dispersed flow, respectively. The values estimated by the images was always higher than those measured with the capacitance system. The explanations are: (1) the capacitive measurement system can record tridimensional fluctuations, but the camera-based imaging technique only record 2D information, (2) distortions related to problems about keeping the focus of the camera on the diametrical-vertical plane and 3) image segmentation errors.

Acknowledgements

The authors are grateful to CAPES (Coordenação de Aperfeiçoamento de Pessoal de Nível Superior) and CNPq (Conselho Nacional de Desenvolvimento Científico e Tecnológico) for the PhD grant and research productivity grant, respectively. The authors are also grateful to Hélio Trebi for his support and contribution in part of the experimental work.

Appendix A. Supplementary data

Supplementary data to this article can be found online at https://doi.org/10.1016/j.flowmeasinst.2019.02.007.

References

[1] U.S. Energy Information Administration, EIA - International Energy Outlook 2016, (2016) https://www.eia.gov/outlooks/ieo/world.cfm , Accessed date: 9 May 2017[Online]. Available: https://www.eia.gov/outlooks/ieo/world.cfm.

[2] A.R. Gurgel, A.R. Diniz, E.A. Araújo, E.R.V.P. Galvão, M.A.F. Rodrigues, T.V. D Jr., Economical evaluation of heavy oil production from the Brazilian Northeast, Energy Sources B Energy Econ. Plan. Policy 12 (2) (2017).

[3] A.C. Bannwart, Modeling aspects of oil – water core – annular flows, J. Pet. Sci. Eng. 32 (2001) 127–143.

[4] O.M.H. Rodriguez, a. C. Bannwart, C.H.M. de Carvalho, Pressure loss in core-annular flow: modeling, experimental investigation and full-scale experiments, J. Pet. Sci. Eng. 65 (1–2) (Mar. 2009) 67–75.

[5] I.H. Rodriguez, H.K.B. Yamaguti, M.S. De Castro, M.J. Da Silva, O.M.H. Rodriguez, Drag reduction phenomenon in viscous oil-water dispersed pipe Flow : experimental investigation and phenomenological modeling, AIChE J. 58 (9) (2012) 2900–2910.

[6] A. Hart, A review of technologies for transporting heavy crude oil and bitumen via pipelines, J. Pet. Explor. Prod. Technol. 4 (3) (2014) 327–336.

[7] R.G. Santos, W. Loh, a. C. Bannwart, O.V. Trevisan, An overview of heavy oil properties and its recovery and transportation methods, Braz. J. Chem. Eng. 31 (3) (2014) 571–590.

[8] A.C. Bannwart, O.M.H. Rodriguez, J.L. Biazussi, F.N. Martins, M.F. Selli, C.H.M. De Carvalho, Water-assisted flow of heavy oil in a vertical pipe: pilot-scale experiments, Int. J. Chem. React. Eng. 10 (2011) A32.

[9] D.M. Rocha, C.H.M. de Carvalho, V. Estevam, O.M.H. Rodriguez, Effects of water and gas injection and viscosity on volumetric fraction, pressure gradient and phase inversion in upward-vertical three-phase pipe flow, J. Pet. Sci. Eng. 157 (2017) 519–529 July.

[10] O.M.H. Rodriguez, A.C. Bannwart, Stability analysis of core-annular flow and neutral stability wave number, AIChE J. 54 (1) (2008) 20–31.

[11] O.M.H. Rodriguez, A.C. Bannwart, Experimental study on interfacial waves in vertical core flow, J. Pet. Sci. Eng. 54 (3–4) (2006) 140–148.

[12] R.V.A. Oliemans, G. Ooms, H.L. Wu, A. Duijvestijn, Core-annular oil/water flow: turbulent -Lubricanting-Film model and measurement in a 5cm pipe loop, Int. J. Multiph. Flow 13 (1) (1987) 23–31.

[13] M.S. Arney, R. Bai, E. Guevara, D.D. Joseph, K. Liu, Friction factor and holdup studies for lubricated pipelining–i, Int. J. Multiph. Flow 19 (6) (1993) 1061–1076.

[14] B. Grassi, D. Strazza, P. Poesio, Experimental validation of theoretical models in two-phase high-viscosity ratio liquid – liquid flows in horizontal and slightly inclined pipes, Int. J. Multiph. Flow 34 (2008) 950–965.

[15] G. Sotgia, P. Tartarini, E. Stalio, Experimental analysis of flow regimes and pressure drop reduction in oil–water mixtures, Int. J. Multiph. Flow 34 (12) (Dec. 2008) 1161–1174.

[16] D. Strazza, B. Grassi, M. Demori, V. Ferrari, P. Poesio, Core-annular flow in horizontal and slightly inclined pipes: existence, pressure drops, and hold-up, Chem. Eng. Sci. 66 (12) (Jun. 2011) 2853–2863.

[17] D. Strazza, M. Demori, V. Ferrari, P. Poesio, Capacitance sensor for hold-up measurement in high-viscous-oil/conductive-water core-annular flows, Flow Meas. Instrum. 22 (5) (Oct. 2011) 360–369.

[18] D. Strazza, P. Poesio, Chemical engineering research and design experimental study

on the restart of core-annular flow, Chem. Eng. Res. Des. 90 (11) (2012) 1711–1718.
[19] E.M.R.M.I. Housz, G. Ooms, R.A.W.M. Henkes, M.J.B.M. Pourquie, A. Kidess, R. Radhakrishnan, A comparison between numerical predictions and experimental results for core-annular flow with a turbulent annulus, Int. J. Multiph. Flow 95 (2017).
[20] A.C. Bannwart, O.M.H. Rodriguez, C.H.M. de Carvalho, I.S. Wang, R.M.O. Vara, Flow patterns in heavy crude oil-water flow, J. Energy Resour. Technol. 126 (3) (2004) 184.
[21] A.C. Bannwart, O.M.H. Rodriguez, J.L. Biazussi, N. Fabio, "Water-Assisted flow of heavy oil in a vertical Pipe : pilot -scale experiments, 12TH International Conference Multiphase Flow in Industrial Plants, 2011, pp. 1–12.
[22] S. Ghosh, T.K. Mandal, G. Das, P.K. Das, Review of oil water core annular flow, Renew. Sustain. Energy Rev. 13 (8) (Oct. 2009) 1957–1965.
[23] A.C. Bannwart, Modeling aspects of oil – water core – annular flows, J. Pet. Sci. Eng. 32 (2001) 127–143.
[24] R. Bai, D.D. Joseph, Steady flow and interfacial shapes of a highly viscous dispersed phase, Int. J. Multiph. Flow 26 (2000) 1469–1491.
[25] R. Martínez-Palou, et al., Transportation of heavy and extra-heavy crude oil by pipeline: a review, J. Pet. Sci. Eng. 75 (3–4) (2011) 274–282.
[26] R. Pal, Mechanism of turbulent drag reduction in emulsions and bubbly suspensions, Ind. Eng. Chem. Res. 46 (2007) 618–622.
[27] A. Omer, R. Pal, Pipeline flow behavior of water-in-oil emulsions with and without a polymeric additive in the aqueous phase, Chem. Eng. Technol. 33 (6) (Jun. 2010) 983–992.
[28] P. Angeli, G.F. Hewitt, Pressure gradient in horizontal liquid-liquid flows, Int. J. Multiph. Flow 24 (7) (1998) 1183–1203.
[29] J. Lovick, P. Angeli, "Experimental studies on the dual continuous flow pattern in oil–water flows, Int. J. Multiph. Flow 30 (2) (Feb. 2004) 139–157.
[30] K. Ioannou, O.J. Nydal, P. Angeli, Phase inversion in dispersed liquid–liquid flows, Exp. Therm. Fluid Sci. 29 (3) (Mar. 2005) 331–339.
[31] I.H. Rodriguez, Experimental Study and Modeling of Flow of Inverse Emulsion in Pipes, University of Sao Paulo, 2014.
[32] J.A. Cengel, A. Faruqui, J.W. Finnigan, C.H. Wright, J.G. Kundsen, Laminar and turbulent flow of unstable liquid-liquid emulsions, AIChE J. 8 (3) (1962).
[33] M. Nadler, D. Mewes, Flow induced emulsification in the flow of two immiscible liquids in horizontal pipes, Int. J. Multiph. FlowJ. Multiph. Flow 23 (1) (1997) 55–68.
[34] P. Angeli, G.F. Hewitt, Drop size distributions in horizontal oil-water dispersed flows, Chem. Eng. Sci. 55 (2000) 3133–3143.
[35] J. Lovick, P. Angeli, "Droplet size and velocity profiles in liquid–liquid horizontal flows, Chem. Eng. Sci. 59 (15) (Aug. 2004) 3105–3115.
[36] S.A. Hussain, X.Y. Xu, G.F. Hewitt, Water local volume fraction on oil in water dispersion, J. Appl. Fluid Mech. 1 (2) (2008) 57–63.
[37] H. Li, M. Wang, Y. Wu, G. Lucas, Volume flow rate measurement in vertical oil - in - water pipe flow using electrical impedance tomography and a local probe, 11th International Conference on Multiphase Flow in Industrial Plants, 2008, pp. 293–302 c.
[38] J. Xu, D. Li, J. Guo, Y. Wu, "Investigations of phase inversion and frictional pressure gradients in upward and downward oil–water flow in vertical pipes, Int. J. Multiph. Flow 36 (11–12) (Nov. 2010) 930–939.
[39] I.H. Rodriguez, H.K.B. Yamaguti, M.S. de Castro, M.J. Da Silva, O.M.H. Rodriguez, "Slip ratio in dispersed viscous oil–water pipe flow, Exp. Therm. Fluid Sci. 35 (1) (Jan. 2011) 11–19.
[40] H. Schümann, M. Tutkun, Z. Yang, O.J. Nydal, Experimental study of dispersed oil-water flow in a horizontal pipe with enhanced inlet mixing, Part 1 and 2, J. Pet. Sci. Eng. 145 (September) (2016) 742–762.
[41] A. Bonilla Riaño, A.C. Bannwart, O.M.H. Rodriguez, Film thickness planar sensor in oil-water flow: prospective study, Sens. Rev. 35 (2) (Mar. 2015) 200–209.
[42] A. Bonilla Riaño, A. Bannwart, H.F. Velasco, O.M.H. Rodriguez, H.-M. Prasser, Film thickness measurement system using FPGA technology, 2015 20th Symposium on Signal Processing, Images and Computer Vision, STSIVA), 2015, pp. 1–7.
[43] M.J. Da Silva, Impedance Sensors for Fast Multiphase Flow Measurement and Imaging, TUDpress, 2008.
[44] R. Tiwari, M. Damsohn, H.-M. Prasser, D. Wymann, C. Gossweiler, Multi-range sensors for the measurement of liquid film thickness distributions based on electrical conductance, Flow Meas. Instrum. 40 (2014) 124–132.
[45] A. Sihvola, Electromagnetic Mixing Formulas and Applications, Institution of Engineering and Technology, 1999.
[46] J.G. Flores, X.T. Chen, C. Sarica, J.P. Brill, Characterization of oil-water flow patterns in vertical and deviated wells, SPE Prod. Facil. 14 (02) (May 1999) 94–101.
[47] A. Bonilla Riaño, H. Velasco Peña, O.M.H. Rodriguez, A. Bannwart, High spatial and temporal resolution film thickness planar sensor: comparison of geometries, Sens. Rev. 39 (1) (2018) 78–86.
[48] A. Bonilla Riaño, I.H. Rodriguez, A.C. Bannwart, O.M.H. Rodriguez, Film thickness measurement in oil–water pipe flow using image processing technique, Exp. Therm. Fluid Sci. 68 (2015) 330–338.